A Gradual Increase of Iron Toward the Medial-Inferior Tip of the Subthalamic Nucleus

Gilles de Hollander,[1] Max C. Keuken,[1,2] Pierre-Louis Bazin,[2] Marcel Weiss,[2] Jane Neumann,[2,3] Katja Reimann,[2] Miriam Wähnert,[2] Robert Turner,[2] Birte U. Forstmann,[1]* and Andreas Schäfer[2]

[1]University of Amsterdam, Amsterdam Brain Center, Amsterdam, the Netherlands
[2]Max Planck Institute for Human Cognitive and Brain Sciences, Leipzig, Germany
[3]Leipzig University Medical Center, IFB Adiposity Diseases, Leipzig, Germany

◆   ═══════════════════════════════════   ◆

Abstract: The subthalamic nucleus (STN) is an important node of the cortico-basal ganglia network and the main target of deep brain stimulation (DBS) in Parkinson's disease. Histological studies have revealed an inhomogeneous iron distribution within the STN, which has been related to putative subdivisions within this nucleus. Here, we investigate the iron distribution in more detail using quantitative susceptibility mapping (QSM), a novel magnetic resonance imaging (MRI) contrast mechanism. QSM allows for detailed assessment of iron content in both in vivo and postmortem tissue. Twelve human participants and 7 postmortem brain samples containing the STN were scanned using ultra-high field 7 Tesla (T) MRI. Iron concentrations were found to be higher in the medial-inferior tip of the STN. Using quantitative methods we show that the increase of iron concentration towards the medial-inferior tip is of a gradual rather than a discrete nature. *Hum Brain Mapp 00:000–000, 2014.* © **2014 Wiley Periodicals, Inc.**

Key words: subthalamic nucleus; quantitative susceptibility mapping; iron gradients; 7T MRI

◆   ═══════════════════════════════════   ◆
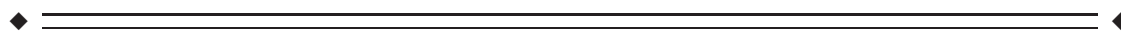
INTRODUCTION

In this study, the spatial distribution of iron in the STN was investigated using ultra-high resolution 7T MRI and QSM of both in vivo and postmortem brains. QSM is a novel MR contrast mechanism that provides a map of local tissue magnetic susceptibility, which allows for the quantification of iron content [Deistung et al., 2013; Langkammer et al., 2012; Schweser et al., 2011].

In the basal ganglia (BG), and more specifically the STN, iron is present in relatively high concentrations as compared to other brain areas [Aquino et al., 2009; Deistung et al., 2013; Schäfer et al., 2011]. Previous histochemical work has shown that iron is heterogeneously distributed in the STN and that a close relationship exists between iron and cytoarchitectonic features [Dormont et al., 2004; Fiedler et al., 2007; Massey et al., 2012].

The heterogeneous distribution of iron might be related to functional subdivisions in the STN, in line with the influential tripartite model of a (oculo)motor, associative, and limbic networks within the BG [e.g., Alexander and Crutcher, 1990]. In one interpretation of this tripartite hypothesis, the iron-rich medial part of the STN should be related to the limbic circuit, an intermediate level of iron should be found in the associative network, and the
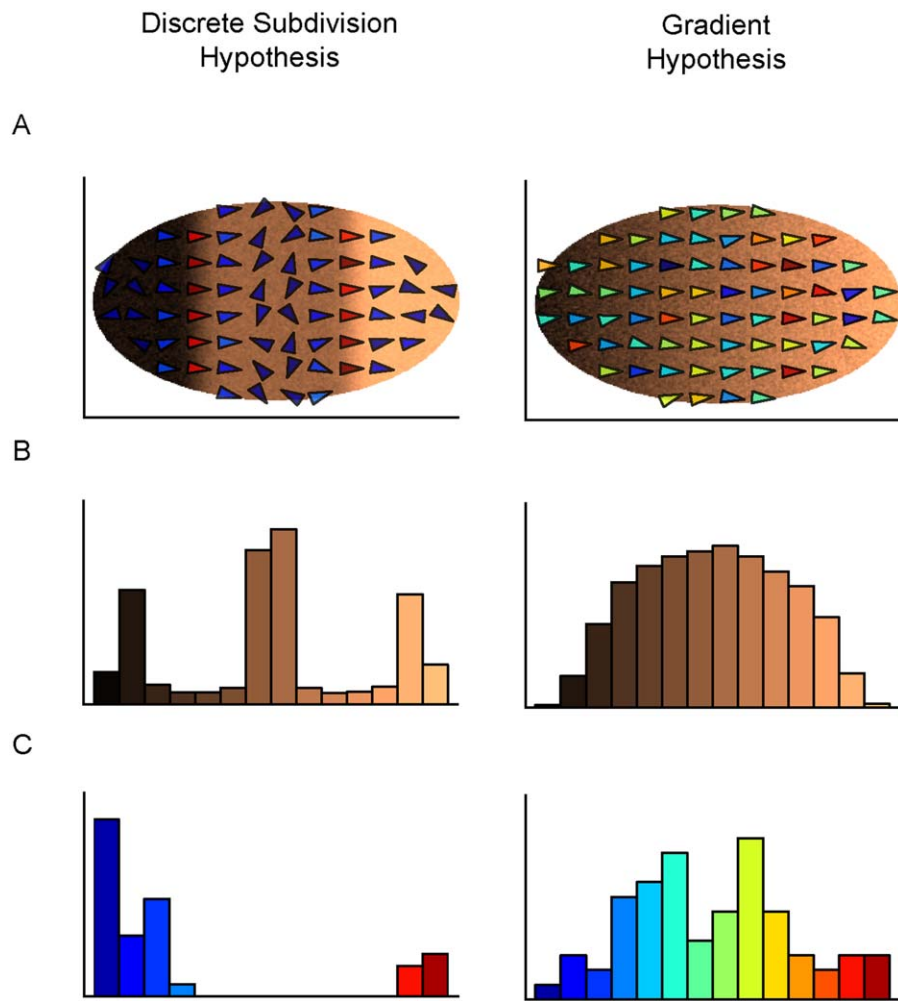
Figure 1.

Hypothetical distributions of iron: (**A**) Simulated (2D) data of both the discrete subdivisions and gradient hypothesis. The copper color map indicates iron concentration, the arrows the direction of the gradient and their color the size of the gradient. (**B**) Histograms of raw intensity values. According to the discrete subdivision hypothesis, multiple clusters of susceptibility values should be present. According to the gradient hypothesis, only a single cluster of values is present. (**C**) Distribution of gradient vector lengths. According to the discrete subdivision hypothesis, a small fraction of the vector lengths is much higher and the distribution is bimodal. According to the gradient hypothesis, the vector lengths are distributed unimodal.

posterior-lateral sensorimotor part should reveal the lowest concentration of iron [Dormont et al., 2004]. The tripartite hypothesis is at odds with a recently conducted literature review revealing an inconsistent pattern of the precise number and location of subdivisions in both humans and non-human primates [Keuken et al., 2012]. This inconsistency in the literature might be rooted in the assumption of sharp borders between the projections of functionally distinct circuits in such small nuclei. Instead of discrete subdivisions, projections of distinct networks to the STN might largely overlap and are organized in a continuous manner similar to the striatum [Alkemade, 2013; Haber, 2003]. Such a model is in line with recent findings that argue for a convergence rather than discrete functional bounds within the STN [Haynes and Haber, 2013] and follows the model previously proposed by Alexander et al. [1986].

Here, iron concentrations in the STN were used as a proxy to test two opposing hypotheses: (a) that there are discrete subdivisions of iron distribution in the STN; (b) there is a gradual increase of iron distribution in the STN. These hypotheses make different predictions about the shape of the magnetic susceptibility distributions displayed in QSM as well as the size of the vectors in the gradient field of the QSM (see Fig. 1 for a simulation of these

TABLE I. Demographics of the postmortem tissue

Brain	Sex	Age	Hemisphere	Cause of death	PMD (hours)	Resolution MRI
1	M	88	L	Aortic stenosis, hypertension, hypercholesterolemia, cardiorenal syndrome, ischeamic cardiomyopathy, atrial fibrillation, rupture of the bowel.	6	0.2 mm^3
2	F	101	L	Hypertension, old myocardial infarction, stomach carcinoma, metastasized, reflux oesophagitis, anemia, coxarthrosis, respiratory insufficiency	5	0.2 mm^3
3	F	91	L	Cardiac insufficiency, urinary tract infection, bronchitis	22	0.2 mm^3
			R			0.2 mm^3
4	F	70	L	Cardiac decompensation	28	0.15 mm^3
			R			0.15 mm^3
5	M	62	L	Sepsis	36	0.15 mm^3
			R			0.15 mm^3

PMD: postmortem delay.

two models). In case of discrete boundaries, a multimodal distribution of iron concentration is expected (Fig. 1b), as well as the presence of a subset of relatively large gradient vectors (Fig. 1c), reflecting a large increase of iron concentration over small distances. In case of a gradual increase of iron concentrations, a unimodal distribution of both iron concentration and gradient vectors is expected.

In the following we will test these different predictions and show using quantitative measures that there is a consistent increase of iron toward the medial-inferior tip of the STN, but that this increase is of a gradual nature.

METHODS

MR Acquisition Protocol and Segmentation of the STN

In vivo data

Thirteen healthy young participants (mean age 24.38 years old, range 22–28 years, standard deviation 2.36, six females) were scanned on a 7T Magnetom MRI system (Siemens, Erlangen) using a 24-channel head array Nova coil (NOVA Medical, Wilmington, MA). The study was approved by the local ethics committee at the University of Leipzig, Germany. All subjects gave their written informed consent prior to scanning and were given a monetary compensation. One participant had to be excluded due to problems with the orientation of the acquisition matrix, which resulted in uncertainty regarding the anatomical orientation. Whole brain images were acquired with an MP-RAGE [Deichmann et al., 2000] sequence (TR = 3,000 ms, TE = 2.95 ms, TI = 1,100 ms, voxel size: 0.8 mm isotropic, flip angle = 6°, GRAPPA acceleration factor 2). Moreover, multiecho spoiled three dimensional (3D) gradient echo images (GRE) FLASH [Elolf et al., 2007; Frahm et al., 1986] sequence (TR = 43 ms, TE = 11.22/ 21.41/31.59 ms, flip angle = 13°, voxel $0.5 \times 0.5 \times 0.6$ mm^3, 56 coronal slices) were acquired. Subsequently, individual QSM of the STN were calculated in the following way: First, the phase images of the FLASH data, which show the field perturbations of a magnetic susceptibility distribution [Schäfer et al., 2009], were unwrapped using a best-path 3D unwrapping algorithm [Abdul-Rahman et al., 2007]. Second, the unwrapped phase data were converted in units of ppm and highpass-filtered using the SHARP algorithm [Schweser et al., 2011]. To calculate the magnetic susceptibility distribution from filtered phase data, the approach of inversion of the thresholded dipole kernel was applied [Wharton et al., 2010].

Postmortem data

Postmortem tissue blocks obtained from five human brains were scanned on a 7T Magnetom MRI system (Siemens, Erlangen) with a dedicated in-house built RF coil for small tissue samples. For three of the five brains tissue blocks both hemispheres were available resulting in five left and three right STNs in total.

Two tissue blocks were obtained from the Netherlands Brain Bank in Amsterdam, the Netherlands (http://www. brainbank.nl/). The remaining postmortem tissue blocks were obtained from the Max Planck Institute for Human Cognitive and Brian Sciences, Leipzig, Germany. All postmortem tissue was obtained in accordance with all legal requirements. Tissue blocks were fixed in 4%

formaldehyde for ~30 days prior to 7T MRI scanning. See Table I for the clinico-pathological data of the postmortem tissue.

The tissue blocks were placed in an acrylic sphere filled with Fomblin® (Solvay Solexis, West Deptford, NJ), a highly viscous fluid of perfluoropolyethers, to avoid background signal. All tissue blocks were scanned using a GRE FLASH sequence (three tissue blocks were scanned with TE = 10 ms, TR = 30 ms, bandwidth = 100 Hz/px, angle = 10°, voxel size = 0.2 mm^3; two tissue blocks were scanned with TE = 7 ms, TR = 23 ms, bandwidth = 120 Hz/px, angle = 30°, voxel size = 0.15 mm^3;). Three different orientations of each tissue sample to the main magnetic field were acquired by rotating each sample around the left-right axis of +60 degrees and −60 degrees. The phase information of the resulting three FLASH datasets were unwrapped using best-path 3D unwrapping algorithm [Abdul-Rahman et al., 2007]. The magnitude images of the FLASH data sets were coregistered using SPM and the registration matrices were applied to the unwrapped phase data. The coregistered phase data were highpass-filtered using a fourth order polynomial and converted in units of ppm. The QSM were calculated using the COSMOS approach and the phase data of the three different orientations for each tissue block [Liu et al., 2009].

Manual segmentation of the subthalamic nucleus

Manual segmentation was performed using the FSL 4.1.4 viewer. Segmentation was carried out by two independent researchers. Subsequently, the inter-rater agreement was assessed. Only voxels rated by both raters as belonging to the STN were included in further analyses. Inter-rater reliability for the manual segmentation was assessed using the Dice coefficient [Dice, 1945]. For more detailed information regarding the segmentation protocol, see [Forstmann et al., 2012; Keuken et al., 2013].

Analyses of Iron Distribution

To allow for earlier findings to be replicated and distinguish between the two main hypotheses of (a) discrete subdivisions, or (b) a gradual increase of iron within the STN (Fig. 1), QSM and quantitative gradient vector analyses was performed. After the QSM contrast was constructed, the gradient vector field of the QSM was estimated. Such a field indicates, for every voxel, the direction in which the largest increase of iron concentration is present as well as the magnitude of this increase.

Both hypotheses predict a single direction of iron increase. To test whether this was a plausible assumption for further analyses, the QSM data were tested for one or more gradient directions using the most likely number of clusters according to a spherical clustering algorithm [Maitra and Ramler, 2010]. Second, the direction of the mean gradient vector was computed. This mean vector reflects the main direction of the overall increase in iron and

allowed the quantitative replication of earlier qualitative findings of increased iron concentrations in the anterior-medial tip of the STN [Dormont et al., 2004; Massey et al., 2012]. Third, to distinguish between the two main hypotheses, k-means clustering was performed on the raw QSM values as well as the gradient vector lengths (Fig 1).

Gradient vector field estimation in the QSM

The derivatives of the QSM were estimated over all three axes (I_x, I_y and I_z). This was done by convolution with a Gaussian first derivative-operator [Lohmann, 1998; Solem, 2012; Szeliski, 2010], with an absolute sigma of 1.5 times the voxel width of the in vivo data. To prevent the occurrence of any spurious gradients as a result of differences in intensity with voxels partly outside the STN (partial volume effects), the masks were eroded by one voxel. All voxels outside the resulting masks were interpolated with the magnetic susceptibility value of their nearest neighbor within the mask to ensure that no gradients were rooted in susceptibility values outside the mask. This procedure yielded a vector field indicating the main direction and size of the derivative of the image at every voxel inside the STN.

Number of distinct gradient vector field directions

To assess whether a single direction of iron increase was plausible, a spherical k-means algorithm was applied to all gradient direction vectors of the QSM gradient vector field within the STN-mask. The likelihoods of different numbers of orientation clusters were assessed using a formal version of the "elbow method" proposed by Maitra and Ramler [2010].

Anatomical regularity

To test for a regular pattern in gradient direction within the sample population, the k main gradient directions according to the maximum likelihood of the spherical k-means algorithms were binned in an eight-bin orientation histogram which was tested for uniformity using a χ^2-test and plotted on a Lambert plane for visual inspection [Mardia and Jupp, 2000, Chapter 9].

Susceptibility distributions and gradient vector length clustering

To test for distinct clusters of iron concentrations, as predicted by the discrete subdivision hypothesis (Fig. 1b), a standard k-means algorithm [MacQueen, 1967; Maechler et al., 2013] was applied to the one-dimensional vector containing the susceptibility values of all voxels within the STN mask. The optimal number of clusters was determined using the gap statistic proposed by Tibshirani [2001].

To test for the presence of any sharp boundaries, as predicted by the discrete subdivision hypothesis (Fig. 1c), the sizes of the gradient vectors were also clustered using the
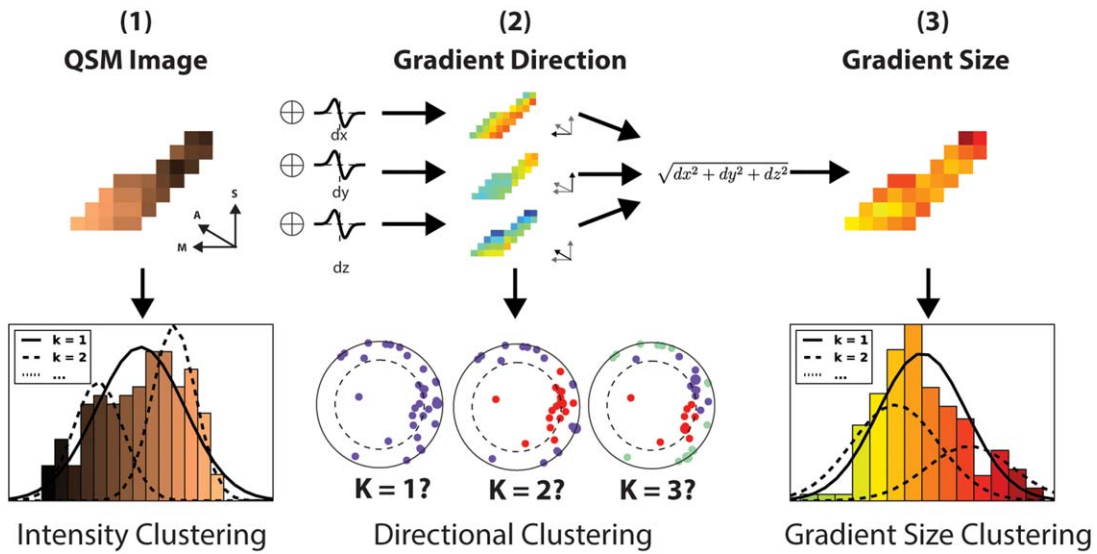
Figure 2.

Overview of the analysis pipeline. (**A**) The input of the pipeline is the QSM image which quantifies the magnetic susceptibility for each voxel and thus the iron content in basal ganglia regions. The susceptibility values are then clustered. (**B**) The QSM is convolved with the derivative of a Gaussian separately in all three directions. This yields a vector field indicating, for each voxel, in which direction the iron increases most. These directions are also clustered. (**3**) Finally, the length of the gradient vectors is calculated and clustered. Plots in this figure are constructed using the actual QSM data of a representative subject of the in vivo dataset.

same k-means algorithm and gap statistic. See Figure 2 for a visual representation of the analysis pipeline.

RESULTS

Inter-rater Reliability Coefficients of the STN Masks

Across the in vivo participants and hemispheres, the mean (SD) Dice coefficient varied between 0.43 and 0.85 with a mean of 0.73 (0.09). Across the remaining postmortem STN tissue and hemispheres the mean (SD) Dice coefficient varied between 0.74 and 0.87 with a mean of 0.83 (0.05). For one of the tissue blocks, i.e., the right STN of case no.3 (see Table I), both raters agreed on a STN overlap of only 20 mm³. Given this very small volume, this sample was excluded from any further analysis. In summary, both the in vivo and postmortem inter-rater reliability coefficients showed a high overlap across raters. See Figure 3 for a representational in vivo and postmortem QSM scan of the STN.

Number of Gradients in the Vector Directions

According to the spherical clustering algorithm, a single direction of iron increase across the STN, as predicted by both hypotheses, seemed plausible for the large majority of the data. In the in vivo data, in the left hemisphere,

$k = 1$ was the most likely model for 9 out of 12 participants. For the remaining three participants, $k = 2$ was found to be the most likely number of clusters. In the right hemisphere, for 11 participants a single cluster was the most likely and for 1 participant, $k = 2$ was the most likely number of clusters. When clustering the gradient vectors in the postmortem data, 7 out of the 7 postmortem samples showed $k = 1$ as the most likely number of distinct gradients. See Supporting Information Table I for the explained variance per k number of gradient clusters.

Consistency of the Main Iron Gradient Direction Across Participants

The consistency of the main iron gradient direction across participants was tested by plotting the cluster centroids for the most likely number of clusters together on a Lambert azimuthal equal-area projection circle. In such a projection, the surface of a sphere is represented as a circle where relative area is preserved [Mardia and Jupp, 2000, Chapter 9]. As can be seen in Figure 4, the main direction of the iron gradient, for both the in vivo data sets and postmortem tissue and both in left and right STN, lie in the medial-inferior direction: iron concentrations increase towards the medial-inferior tip of the STN.

To quantitatively assess whether the distribution of the main gradient directions over participants and postmortem tissue was nonuniform and consistent, we divided the
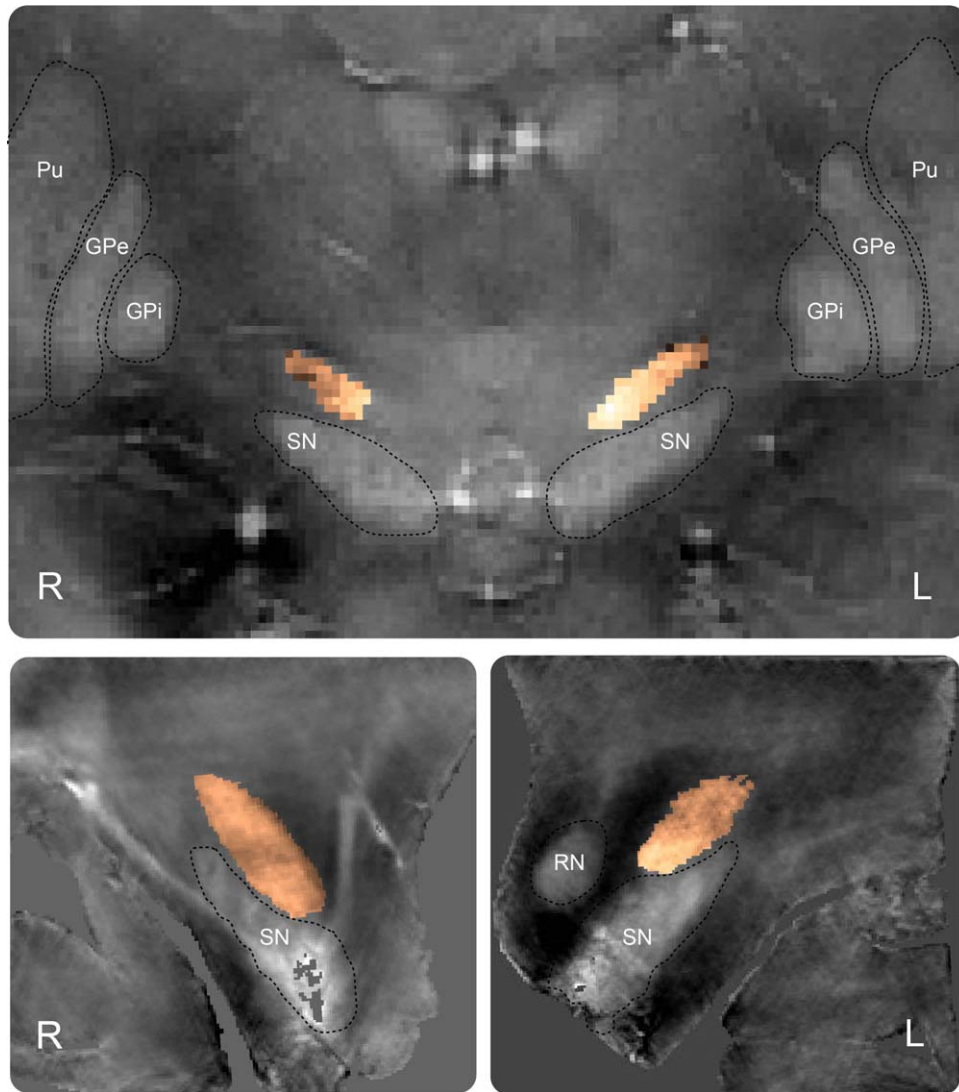
Figure 3.

QSM-images of the STN in vivo and postmortem. (Upper panel) QSM-image of a single in vivo participant. Superimposed on the scan are the raw QSM values for the STN mask in copper. Lower two panels) QSM images of a right and left hemisphere tissue block of an ex vivo sample. Superimposed on the scans are the raw QSM values for the STN in copper. Note that the voxel size of the ex vivo sample is about 37 times smaller than the voxel size of the in vivo sample ($0.15 \times 0.15 \times 0.15$ mm^3 vs. $0.5 \times 0.5 \times 0.5$ mm^3). Pu: putamen, GPe: globus pallidus externa, GPi: globus pallidus interna, SN: substantia nigra, RN: red nucleus.

unit sphere in eight bins of equal surface representing the $2^3 = 8$ possible combinations of the axes medial vs. lateral, anterior vs. posterior, and inferior vs. superior. A chi-squared test shows that in the in vivo-data, in both hemispheres the main directions are not uniformly distributed over the eight direction bins ($\chi^2(7, N = 15) = 20.73, p = .0042$) for the left STN, and ($\chi^2(7, N = 13) = 15.92, p = .026$) for the right STN, where for both hemispheres the medial-inferior direction was the preferred direction. In summary, the direction of the individual iron gradient is consistent.

The small number of postmortem cases did not allow the computation of chi-squared test.

Susceptibility Distribution and Gradient Vector Length Clustering

The discrete subdivision hypothesis predicts that multiple discrete clusters of similar susceptibility values exist. However, k-means clustering on the raw QSM yielded
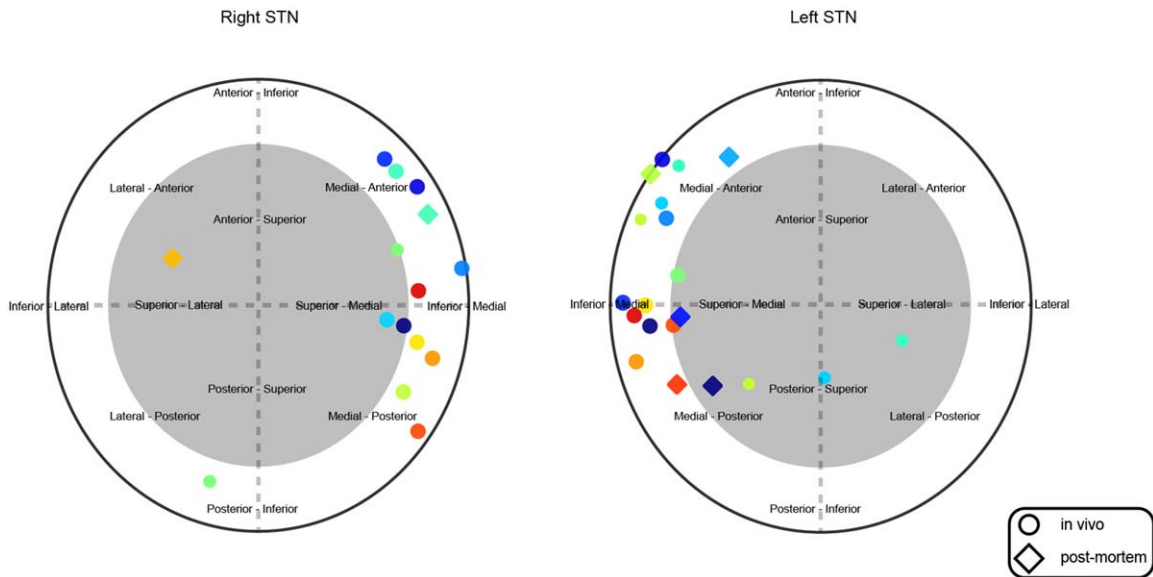
Figure 4.

Main directions of the iron gradient for in vivo and postmortem data. Every point represents one of the main directions of iron gradients in the left and right STN mask. Markers with the same color and glyph are main directions within the same sample when $k = 2$ was the most likely model (4 out of 24 cases). The size of the glyphs represents the size of the gradient cluster. The diamond glyphs represent the postmortem brain.

$k = 1$ as the most likely number of clusters in all 12 in vivo data sets, for both the left and right hemispheres. The postmortem data also showed $k = 1$ as the most likely number of clusters in all seven postmortem samples. These analyses suggest a gradual increase of iron rather than discrete boundaries. See Supporting Information Table II for the maximum likelihood per k number of QSM susceptibility value clusters.

For the gradient vector lengths, the discrete hypothesis predicts a multimodal distribution of gradient vector magnitudes with a distinct subset of gradient vectors of large magnitude. Clustering on the magnitudes of the gradient vectors using k-means showed $k = 1$ as the most likely number of clusters in all 12 in vivo data sets in both hemispheres and all seven postmortem tissues. In summary, both in vivo and postmortem data confirm the gradient hypothesis. See Supporting Information Table III for the maximum likelihood per k number of the gradient vector length clusters.

DISCUSSION

The present study replicates and extends previous findings of heterogeneous iron distributions throughout the STN [Dormont et al., 2004; Massey et al., 2012] by using ultra-high resolution 7T quantitative susceptibility MR mapping of both in vivo subjects and postmortem tissue. Single iron gradients, mainly pointing in the

medial-inferior direction, were found in the majority of the samples (7/7 in postmortem, 9/12 for left and 11/12 for right in vivo STN).

Complementary to the findings of Dormont et al. [2004] and Massey et al. [2012] who reported an increase in iron in the medial-anterior direction, here we show increased iron concentrations in the medial-inferior-anterior direction. This difference might be due to the different methodologies employed in the aforementeiond studies, as both Dormont et al. [2004] and Massey et al. [2012] used histological staining on a limited number of specimens and reported the topology of the employed stainings only qualitatively. Also, histological work is always confined to a single cutting plane eventually inducing biases of changes in intensities in one axis of the plane. Any gradients in the inferior-superior axis will especially be less evident when axial sections are used, as was done in Massey et al. [2012]. In Dormont et al. [2004], coronal sections were used so that inferior gradients should be more visible, however, only one single specimen was investigated. Both anatomical variability and the lack of any quantitative measures might explain that an inferior gradient was not found in the Dormont study. Here we present quantitative analyses in the intact STN in 3D on a much larger number of specimens which suggest a similar pattern of increased iron as the abovementioned studies and complementing these findings with the presence of an inferior component to the iron gradient.

Importantly, this quantitative approach allowed the testing of two hypotheses regarding the functional organization of the STN using the iron distribution as a proxy: (a) the discrete subdivision hypothesis, and (b) the gradient hypothesis. *K*-means clustering analysis of the QSM susceptibility values showed no discrete clusters of iron intensities. In addition, the *k*-means clustering analysis of the gradient vector lengths revealed that there are no sharp boundaries or septa within the STN. Note that these analyses are agnostic towards the number of possible subdivisions because they only reveal a lack of distinct boundaries.

These findings are in favor of the second hypothesis of a gradual increase in iron. We suggest that this reflects that projections of different cortical networks, such as the motor, cognitive, and limbic system converge in the STN and largely overlap, as argued before by Haynes and Haber [2013]. This makes sense in light of the integrative function of the STN: a relatively small nucleus, but with a wide array of projections from almost the entire cortex as well as many subcortical areas [Lambert et al., 2012; Temel et al., 2005a]. It is, however, at odds with the well-known but inconclusive tripartite subdivision model segregating (oculo)motor, cognitive, and limbic networks (see, e.g., Alexander and Crutcher, 1990; Alexander et al., 1986, 1991; DeLong et al., 1985; Hamani et al., 2004; Joel and Weiner, 1997; Krack et al., 2010; Nakano, 2000; Obeso et al., 2008; Parent and Hazrati, 1993, 1995a,b; Parent, 1990; Rodriguez-Oroz et al., 2001, 2009; Temel et al., 2005b).

Finally, a gradual organization of iron within the STN could have important clinical implications, in particular for the electrode placement in deep brain stimulation (DBS) in Parkinson's patients. DBS of the STN can cause serious "cognitive" and "limbic" side-effects, theorized to be due to disturbance of the limbic and associative networks as opposed to the motor network within the STN [Temel et al., 2005a]. If these different networks largely overlap within this nucleus, it could be possible to minimize non-motor side effect in DBS by avoiding the region that is least connected to motor-related areas [Lambert et al., 2012]. However, it still remains unclear how large these functional areas or transitional zones between areas are. Should the overlap be substantial then it will be significantly more challenging to devise a surgical solution that minimizes non-motor side effects.

Limitations

Two limitations will be discussed in this section. First, iron is just one of many heavy metal markers of the structural organization in the subcortex. It is possible that other markers such as zinc and copper could show a different distribution. However, there is evidence for a close relationship between iron and cytoarchitectonic features and thereby potentially revealing anatomical subdivisions [Fiedler et al., 2007]. Second, iron plays a role in a range of brain functions including myelin production, oxygen transport, and neurotransmitter synthesis [Rouault, 2001; Zecca et al., 2004]. Complementary to the role iron plays in cellular functions, there is some evidence linking levels of iron in subcortical structures to higher-level cognitive functions [Penke et al., 2012; Sullivan et al., 2009]. It is thus likely that a gradual distribution of iron in the STN is related to its functional organization.

Third, four out of 24 participants showed more than one gradient orientation cluster. One explanation for these interindividual differences could be the size of the masks, inducing partial volume effects related to the limited resolution compared to the postmortem tissue. Partial volume effects might have yielded gradient vectors pointing into the STN, in particular at the dorsal and ventral borders. These gradients are then exactly opposing each other, and will thus be treated as separate clusters by the clustering algorithm. Argueably, this is an artefact and not an actual property of the iron distribution within the STN. A solution for the removal of these artificially induced clusters is to use additional eroding of the masks. However, we decided to leave the original data as unprocessed as possible to avoid any bias towards one of the two hypotheses.

CONCLUSION

In conclusion, the work presented here shows an increased concentration of iron in the medial-inferior tip of the STN. Iron concentrations in the STN increase gradually towards this tip. It is likely that this gradual increase is related to the functional organization of the STN. The current finding of a gradual organization is at odds with the prominent idea of a one-to-one mapping between clearly discernible cytoarchitectonic areas and specific cognitive functions such as the popular tripartite motor-cognitive-limbic model of the STN [Rodriguez-Oroz et al., 2009]. We propose to update the tripartite motor-cognitive-limbic model of the STN which, in our opinion, should include transition zones as has been previously proposed by several authors [e.g., Alexander et al., 1986; Alkemade, 2013; Haynes and Haber, 2013]. Still, further experiments, including studies of tissue composition and histology are needed in order to provide more insight into the anatomical organization of the STN.

ACKNOWLEDGMENTS

REFERENCES

Abdul-Rahman HS, Gdeisat MA, Burton DR, Lalor MJ, Lilley F, Moore CJ (2007): Fast and robust three-dimensional best path phase unwrapping algorithm. Appl Opt 46:6623–6635.

Alexander GE, Crutcher MD (1990): Functional architecture of basal ganglia circuits: Neural substrates of parallel processing. Trends Neurosci 13:266–271.

Alexander GE, DeLong MR, Strick PL (1986): Parallel organization of functionally segregated circuits linking basal ganglia and cortex. Annu Rev Neurosci 9:357–381.

Alexander GE, Crutcher MD, DeLong MR (1991): Basal ganglia-thalamocortical circuits: Parallel substrates for motor, oculomotor, "prefrontal" and "limbic" functions. Prog Brain Res 85:119–146.

Alkemade A (2013): Subdivisions and anatomical boundaries of the subthalamic nucleus. J Neurosci 33:9233–9234.

Aquino D, Bizzi A, Grisoli M, Garavaglia B, Bruzzone MG, Nardocci N, Savoiardo M, Chiapparini L (2009): Age-related iron deposition in the basal ganglia: Quantitative analysis in healthy subjects. Radiology 252:165–172.

Deichmann R, Good CD, Josephs O, Ashburner J, Turner R (2000): Optimization of 3-D MP-RAGE sequences for structural brain imaging. NeuroImage 12:112–127.

Deistung A, Schäfer A, Schweser F, Biedermann U, Turner R, Reichenbach JR (2013): Toward in vivo histology: A comparison of quantitative susceptibility mapping (QSM) with magnitude-, phase-, and R2-imaging at ultra-high magnetic field strength. NeuroImage 65:299–314.

DeLong MR, Crutcher MD, Georgopoulos AP (1985): Primate globus pallidus and subthalamic nucleus: Functional organization. J Neurophysiol 53:530–543.

Dice LR (1945): Measures of the amount of ecologic association between species. Ecology 26:297–302.

Dormont D, Ricciardi KG, Tandé D, Parain K, Menuel C, Galanaud D, Navarro S, Cornu P, Agid Y, Yelnik J (2004): Is the subthalamic nucleus hypointense on T2-weighted images? A correlation study using MR imaging and stereotactic atlas data. AJNR Am J Neuroradiol 25:1516–1523.

Elolf E, Bockermann V, Gringel T, Knauth M, Dechent P, Helms G (2007): Improved visibility of the subthalamic nucleus on high-resolution stereotactic MR imaging by added susceptibility (T2*) contrast using multiple gradient echoes. Am J Neuroradiol 28:1093–1094.

Fiedler A, Reinert T, Morawski M, Brückner G, Arendt T, Butz T (2007): Intracellular iron concentration of neurons with and without perineuronal nets. Nuclear Instrum Methods Phys Res Sect B Beam Interactions Mater Atoms 260:153–158.

Forstmann BU, Keuken MC, Jahfari S, Bazin P-L, Neumann J, Schäfer A, Anwander A, Turner R (2012): Cortico-subthalamic white matter tract strength predicts interindividual efficacy in stopping a motor response. NeuroImage 60:370–375.

Frahm J, Haase A, Matthaei D (1986): Rapid NMR imaging of dynamic processes using the FLASII technique. Magn Reson Med 3:321–327.

Haber S (2003): The primate basal ganglia: Parallel and integrative networks. J Chem Neuroanat 26:317–330.

Hamani C, Saint-Cyr JA, Fraser J, Kaplitt M, Lozano AM (2004): The subthalamic nucleus in the context of movement disorders. Brain 127:4–20.

Haynes WIA, Haber SN (2013): The organization of prefrontal-subthalamic inputs in primates provides an anatomical substrate for both functional specificity and integration: Implications for basal ganglia models and deep brain stimulation. J Neurosci 33:4804–4814.

Joel D, Weiner I (1997): The connections of the primate subthalamic nucleus: Indirect pathways and the open-interconnected scheme of basal ganglia-thalamocortical circuitry. Brain Res Rev 23:62–78.

Keuken MC, Uylings HBM, Geyer S, Schäfer A, Turner R, Forstmann BU (2012): Are there three subdivisions in the primate subthalamic nucleus? Front Neuroanat 6:14.

Keuken MC, Bazin PL, Schafer A, Neumann J, Turner R, Forstmann BU (2013): Ultra-high 7T MRI of structural age-related changes of the subthalamic nucleus. J Neurosci 33: 4896–4900.

Krack P, Hariz MI, Baunez C, Guridi J, Obeso JA (2010): Deep brain stimulation: From neurology to psychiatry? Trends Neurosci 33:474–484.

Lambert C, Zrinzo L, Nagy Z, Lutti A, Hariz M, Foltynie T, Draganski B, Ashburner J, Frackowiak R (2012): Confirmation of functional zones within the human subthalamic nucleus: Patterns of connectivity and sub-parcellation using diffusion weighted imaging. NeuroImage 60:83–94.

Langkammer C, Schweser F, Krebs N, Deistung A, Goessler W, Scheurer E, Sommer K, Reishofer G, Yen K, Fazekas F, Ropele S, Reichenbach JR (2012): Quantitative susceptibility mapping (QSM) as a means to measure brain iron? A postmortem validation study. NeuroImage 62:1593–1599.

Liu T, Spincemaille P, de Rochefort L, Kressler B, Wang Y (2009): Calculation of susceptibility through multiple orientation sampling (COSMOS): A method for conditioning the inverse problem from measured magnetic field map to susceptibility source image in MRI. Magn Reson Med 61:196–204.

Lohmann G (1998): Volumetric Image Analysis. Wiley, New York.

MacQueen J (1967): Some methods for classification and analysis of multivariate observations. Proceedings of the fifth Berkeley symposium on mathematical statistics and probability 1:281–297.

Maitra R, Ramler IP (2010): A k-mean-directions algorithm for fast clustering of data on the sphere. J Comput Graph Stat 19: 377–396.

Mardia KV, Jupp PE (2000): Directional statistics. 2nd ed. Wiley, New York.

Massey LA, Miranda MA, Zrinzo L, Al-Helli O, Parkes HG, Thornton JS, So PW, White MJ, Mancini L, Strand C, Holton JL, Hariz MI, Lees AJ, Revesz T, Yousry TA (2012): High resolution MR anatomy of the subthalamic nucleus: Imaging at 9.4T with histological validation. NeuroImage 59: 2035–2044.

Maechler M, Rousseeuw P, Struyf A, Hubert M, Hornik K. (2013): Cluster analysis basics and extensions. R package version 1.14.4.

Nakano K (2000): Neural circuits and topographic organization of the basal ganglia and related regions. Brain Dev 22 (Suppl 1): S5–S16.

Obeso JA, Rodríguez-Oroz MC, Benitez-Temino B, Blesa FJ, Guridi J, Marin C, Rodriguez M (2008): Functional organization of the basal ganglia: Therapeutic implications for Parkinson's disease. Mov Disord 23:S548–S559.

Parent A (1990): Extrinsic connections of the basal ganglia. Trends Neurosci 13:254–258.

Parent A, Hazrati LN (1993): Anatomical aspects of information processing in primate basal ganglia. Trends Neurosci 16: 111–116.

Parent A, Hazrati L-N (1995a): Functional anatomy of the basal ganglia. I. The cortico-basal ganglia-thalamo-cortical loop. Brain Res Rev 20:91–127.

Parent A, Hazrati L-N (1995b): Functional anatomy of the basal ganglia. II. The place of subthalamic nucleus and external pallidium in basal ganglia circuitry. Brain Res Rev 20:128–154.

Penke L, Hernandéz MCV, Maniega SM, Gow AJ, Murray C, Starr JM, Bastin ME, Deary IJ, Wardlaw JM (2012): Brain iron deposits are associated with general cognitive ability and cognitive aging. Neurobiol Aging 33:510–517.

Rodriguez-Oroz MC, Rodriguez M, Guridi J, Mewes K, Chockkman V, Vitek J, DeLong MR, Obeso JA (2001): The subthalamic nucleus in Parkinson's disease: Somatotopic organization and physiological characteristics. Brain 124:1777–1790.

Rodriguez-Oroz MC, Jahanshahi M, Krack P, Litvan I, Macias R, Bezard E, Obeso JA (2009): Initial clinical manifestations of Parkinson's disease: Features and pathophysiological mechanisms. Lancet Neurol 8:1128–1139.

Rouault TA (2001): Iron on the brain. Nat Genet 28:299–299.

Schäfer A, Wharton S, Gowland PA, Bowtell RW (2009): Using magnetic field simulation to study susceptibility-related phase contrast in gradient echo MRI. NeuroImage 48:126–137.

Schäfer A, Forstmann BU, Neumann J, Wharton S, Mietke A, Bowtell R, Turner R (2011): Direct visualization of the subthalamic nucleus and its iron distribution using high-resolution susceptibility mapping. Hum Brain Mapp 33:2831–2842.

Schweser F, Deistung A, Lehr BW, Reichenbach JR (2011): Quantitative imaging of intrinsic magnetic tissue properties using MRI signal phase: An approach to in vivo brain iron metabolism? NeuroImage 54:2789–2807.

Solem JE (2012): Programming Computer Vision with Python. Sebastopol, California, USA: O'Reilly Media.

Sullivan E, Adalsensson E, Rohlfing T, Pfefferbaum A (2009): Relevance of iron deposition in deep gray matter brain structures to cognitive and motor performance in healthy elderly men and women: Exploratory findings. Brain Imaging Behav 3:167–175.

Szeliski R (2010): Computer Vision: Algorithms and Applications, 1st ed. New York, NY, USA: Springer-Verlag New York, Inc.

Temel Y, Blokland A, Steinbusch HWM, Visser-Vandewalle V (2005a): The functional role of the subthalamic nucleus in cognitive and limbic circuits. Prog Neurobiol 76:393–413.

Temel Y, Visser-Vandewalle V, Aendekerk B, Rutten B, Tan S, Scholtissen B, Schmitz C, Blokland A, Steinbusch HWM (2005b): Acute and separate modulation of motor and cognitive performance in parkinsonian rats by bilateral stimulation of the subthalamic nucleus. Exp Neurol 193:43–52.

Tibshirani R, Walther G, Hastie T (2001): Estimating the number of clusters in a data set via the gap statistic. J R Stat Soc Ser B (Stat Methodol) 63:411–423.

Wharton S, Schäfer A, Bowtell R (2010): Susceptibility mapping in the human brain using threshold-based k-space division. Magn Reson Med 63:1292–1304.

Zecca L, Youdim MBH, Riederer P, Connor JR, Crichton RR (2004): Iron, brain ageing and neurodegenerative disorders. Nat Rev Neurosci 5:863–873.